

# Chapter 7

## Analyzing Earthquake Events in the Vicinity of Wenchuan Using ETAS Models



Annie Chu

**Abstract** This chapter applies the spatial–temporal epidemic-type aftershock sequence (ETAS) model of Ogata to regional seismicity of surrounding Wenchuan, China. Events between 1973 and 2017 with magnitude 4.0 or above are included for analysis according to the model. The Preliminary Determination of Epicenters (PDE) data used in this study are in a rectangular space window between 98°E and 108°E in longitude and between 26°N and 36°N in latitude. The space window includes the Wenchuan event of May 12, 2008 (epicenter located at 31.021°N, 103.367°E) approximately in the center of the rectangle. We implement five different models, a homogeneous model and four inhomogeneous models, and we compare them in model diagnostics and predicted intensity rate based on MLEs (maximum likelihood estimates), with calculation details provided and emphasized. Additionally, the data in 45 years between 1973 and 2017 are partitioned into two catalogs, before and after the Wenchuan event, and models are built for each catalog for comparison. We have discovered that the seismic activities appear distinct before and after the Wenchuan event, and we describe the difference using the ETAS model with its background rates, triggering parameters and predicted intensity rate. We also implement simulation to provide standard error and confidence interval for each triggering parameter of the best model found among the five models.

**Keywords** Branching-point processes · Earthquake forecasting · Epidemic-type aftershock sequence (ETAS) model · Space-time point process models · Maximum likelihood estimation · EM algorithm · Wenchuan earthquake

---

A. Chu (✉)

Department of Mathematics, Woodbury University, 7500 N. Glenoaks Boulevard, Burbank, CA 91504, USA

e-mail: [aannchu@gmail.com](mailto:aannchu@gmail.com)

## 7.1 Introduction

To study the regional seismicity using data analysis and statistical models, this chapter applies the epidemic-type aftershock sequence (ETAS) model of Ogata (1998) to the regional data of Wenchuan and its vicinity. The ETAS model is a spatial–temporal Hawke’s model to describe the intensity rate of seismicity as the sum of background rate and triggering function. The ETAS model is commonly used for modern seismic analysis on regional data in Japan (Ogata) and Southern California (Veen 2006) and on global data (Chu et al. 2011). It has been used for study of the Wenchuan earthquake on similar rectangular regions, using different time windows of 1970/01/01–2008/05/12 (Jiang and Zhuang 2010) and 1973–2013 (Guo et al. 2015). In this chapter, we provide a robust inhomogeneous model to fit the data to ETAS model. The expectation–maximization (EM) algorithm adopted from Veen and Schoenberg (2008) is modified to seek for the maximum likelihood estimates (MLEs). In order to find an optimal model computationally, MLEs of the parameters are obtained using computer software iteratively. The earthquake catalog data in PDE Web site are chosen for data analysis due to its relative completeness over years. A larger time window of 1973–2017 is used in this chapter.

This chapter is organized as follows. Section 7.2 presents information of the Wenchuan’s vicinity for our computation, and the dataset used for analysis. Section 7.3 introduces the ETAS methods with an emphasis on the computer software used for implementation of inhomogeneous models. Comparison with the background rate is discussed in this section. Section 7.4 presents the result of homogeneous and inhomogeneous modeling. Section 7.5 provides simulation using the parameters obtained in Sect. 7.4 and standard errors of the triggering parameters. Section 7.6 concludes the chapter.

## 7.2 The Study Region and Data

We use the data of PDE in the time window of 45 years from 1973/01/01 to 2017/12/31 in this study. The data analyzed are in the rectangular space window [98°E, 108°E] in longitude by [26°N, 36°N] in latitude. The space window includes the location of the Wenchuan earthquake (31.021°N, 103.367°E), recorded 7.9 in centroid moment magnitude and 8.0 in surface magnitude by the PDE database (Preliminary Determination of Epicenters, USGS 2017), approximately in the center of the rectangular window. We have obtained the data, including 2015 events with magnitudes  $\geq 4.0$ , 250 events with magnitudes  $\geq 5.0$ , and 25 events with magnitude  $\geq 6.0$ . The online PDE database is in fact incomplete for events with magnitude  $< 4.0$ ; the magnitude types of those events are different: Some are moment magnitude some are surface magnitude, etc. The PDE data contain only 338 events with magnitude in the interval between 3.0 and 4.0. Therefore, we exclude events with magnitude  $< 4.0$  in data analysis. Moreover, there are six events with relatively small magnitude  $\leq 4.3$  and at

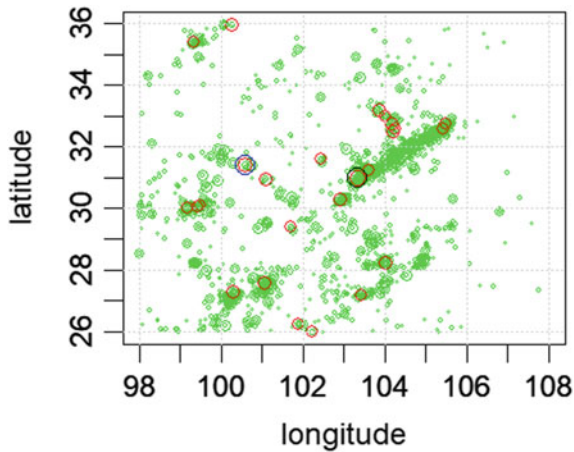


**Fig. 7.1** Events in the space window =  $[98^{\circ}\text{E}, 108^{\circ}\text{E}]$  by  $[26^{\circ}\text{N}, 36^{\circ}\text{N}]$  and time window 1973/01/01 to 2017/12/31. Small green circles indicate events of magnitude 4.0–4.9; large green circles indicate events of magnitude 5.0–5.9. Red circles indicate events of magnitude 6.0–6.9. There are two events of magnitude  $\geq 7.0$ : The large black circle on  $(31.021^{\circ}\text{N}, 103.367^{\circ}\text{E})$  indicates the  $M7.9$  Wenchuan earthquake event in 2008, and the large blue circle indicates the  $M7.4$  Luhuo earthquake in 1973

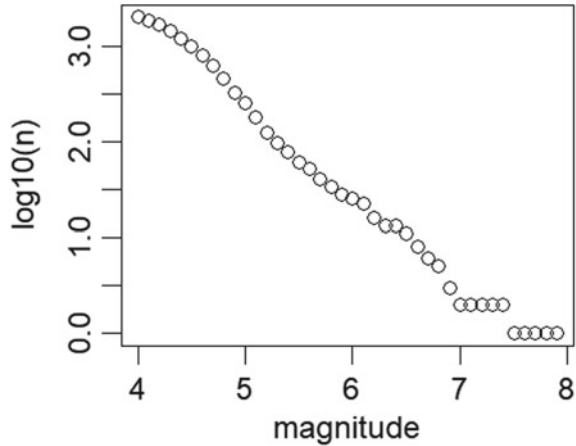
depth  $>70$  km in the PDE online database. To be consistent with global zone data analysis of Chu et al. (2011), we do not use these six deep events and include only shallow events at depth  $\leq 70$  km in this chapter. The Wenchuan event occurred at the depth of 19 km. In time window 1973/01/01–2017/12/31, there are only two events with magnitude  $\geq 7$ : the 2008 Wenchuan event with moment magnitude 7.9 and the Luhuo event with surface wave magnitude 7.4 occurring on 1973/02/06.

The events of magnitudes  $\geq 4.0$  are plotted in Fig. 7.1. We observe that numerous events appear clustered along the stripe of the Longmenshan fault between the Wenchuan mainshock epicenter (at  $31.021^{\circ}\text{N}, 103.367^{\circ}\text{E}$ ) and the northeast end of the Wenchuan aftershock zone (approximately at  $106^{\circ}\text{E}, 33.5^{\circ}\text{N}$ ). However, most of the larger events with magnitudes  $\geq 6.0$  are scattered in Fig. 7.1, and only four of them are located close to the Longmenshan fault. We also observe that the clusters occur around the Longmenshan fault region and around the bottom-left of the study area, but there are not obvious clusters close to the boundary of area, and this minimizes the bias that may be caused by boundary effect in data modeling.

Grouping the data by 0.1 increment in magnitude, we calculate the number of events in each interval of magnitude. In Fig. 7.2, the survivor function is plotted with  $\log_{10}(n)$  versus magnitude, where  $n$  denotes the number of events in intervals magnitude  $\geq 4.0$  (2009 events), magnitude  $\geq 4.1$  (1868 events), magnitude  $\geq 4.2$  (1669 events), etc. The survivor function shows the relation  $\log_{10}(n)$  versus magnitude is roughly linear, and it leads to the data's capability to be modeled by the ETAS model.

The region belongs to the active continent (zone 1) of the four major tectonic zones in Bird's tectonic plate model PB2002 (Birds 2003). Zone 1 includes conti-

**Fig. 7.2** Survival function of the events.  $\log_{10}(n)$  is plotted versus event magnitude where  $n$  is the cumulative number of events. The function is roughly linear, showing near completeness of the seismic catalog



mental parts of all orogens of PB2002 model, plus continental plate boundaries of PB2002) calculated by Chu et al. (2011). Orogens are part of zone 1 based on Bird’s plate boundary model, and it indicates regions of mountain formation or at least topographic roughening. Such regions are difficult to define plates because there is too much seismic, geologic, and geodetic evidence for distributed anelastic deformation (Birds 2003).

This work examines both the estimated Gutenberg–Richter branching ratio 2.6 of zone 1, and the estimated Gutenberg–Richter branching ratio 2.3 provided by Veen (2006) for Southern California earthquake data analysis. The Gutenberg–Richter branching ratio is needed to compute the initial values for the iterated EM algorithm computation, and these two values both lead to the same MLEs in this chapter.

### 7.3 Model and Method

The model used for data analysis in this chapter is the spatial–temporal ETAS model described in Ogata (1998). Since the rectangular region analyzed is in zone 1 of Bird’s tectonic zone (Bird 2003) and one of the three Ogata’s models, model (2.3), appears to fit slightly better for this zone with an only small difference compared to Ogata’s model (2.4) (Chu 2018), we choose this particular model for data fitting in this chapter.

The ETAS model is a type of Hawkes point process model and is also known as branching or self-exciting point process. For such a process with only event time considered, conditional intensity rate at time  $t$ , given history information  $H_t$  of all events prior to time  $t$ , has the form:

$$\lambda(t|H_t) = \mu(x, y) + \sum_{i:t_i < t} g(t - t_i, m_i) \quad (7.1)$$

Ogata's model (2.3) (1998) extends the temporal ETAS model (7.1) to describe the space-time-magnitude distribution of earthquake occurrences by introducing circular or elliptical spatial functions into the triggering function:

$$\lambda(t|H_t) = \mu(x, y) + \sum_{i:t_i < t} g(t - t_i, x - x_i, y - y_i, m_i) \quad (7.2)$$

where  $\mu(x, y) > 0$  denotes the background rate, which may depend on location. A simple case of such model treats  $\mu(x, y)$  as constant. Background events are the events treated as always existing and not being triggered by previous events. The second term  $\sum_{i:t_i < t} g(t - t_i, x - x_i, y - y_i, m_i)$  is the model's triggering part, and it is considered intensity that is triggered by previous events. The nonnegative function  $g(t - t_i, x - x_i, y - y_i, m_i)$  is the triggering function dictating the aftershock activity rate associated with a prior event with time  $t_i$ , location  $(x_i, y_i)$  and magnitude  $m_i$ . Models such as (7.1) are called epidemic by Ogata (1988). In other words, an earthquake can produce aftershock, and the aftershocks produce their aftershocks, and so on.

An example of triggering functions is the time-magnitude ETAS model of Ogata's model (2.3) (1988), which has magnitude-dependent triggering function with the term  $K_0/(t - t_i + c)^p$  describing the temporal distribution of aftershocks and is known as the modified Omori-Utsu law (Utsu et al. 1995):

$$g(t - t_i, x - x_i, y - y_i, m_i) = K_0(t - t_i + c)^{-p} \frac{e^{\alpha(m_i - M_0)}}{((x - x_i)^2 + (y - y_i)^2 + d)^q} \quad (7.3)$$

where the parameter  $\alpha$  describes the influence of magnitude, the smaller  $\alpha$  value indicates more swarm-type seismic activity, and the larger  $\alpha$  value indicates the seismic activity being more clustered. The normalizing constant  $K_0 > 0$  governs the expected number of direct aftershocks triggered by earthquake  $i$ ;  $m_i$  denotes the magnitude of earthquake  $i$ . Events with magnitude less than the lower cutoff  $M_0 = 4$  are excluded. Parameters  $c$  and  $p$  are related to the temporal decay of aftershock activity.  $c$  indicates temporal decay in clustering as an event moves further from the mainshock. The parameter  $p$  governs the temporal distribution of aftershocks. The smaller  $p$  value corresponds to the longer temporal decay while the larger  $p$  value indicates the shorter range decay. Similarly, parameters  $d$  and  $q$  are related to the temporal decay of aftershock activity.  $d$  indicates spatial decay in clustering as an event moves further from the mainshock. The parameter  $q$  governs the spatial distribution of aftershocks. The smaller  $q$  value corresponds to the longer range decay while the larger  $q$  value indicates the shorter range decay (Chu et al. 2011).

The spatial background rate  $\mu(x, y)$  may be treated as homogeneous or inhomogeneous depending on modeling preference and computational feasibility. In this

chapter, we adopt both homogeneous and inhomogeneous models. Many researchers have used various methods to manage the computation of inhomogeneous background rate of the model. For example, Ogata (2011) uses Delaunay tessellation, and Veen and Schoenberg (2008) use manual selection of irregular polygons according to geographic features. The method of adopting irregular polygon requires manual dissection of polygons and might be subjective. In this chapter, we demonstrate a simple implementation of rectangular grids to implement the spatial inhomogeneity part instead of manual selection of polygons. It has the advantage of computation simplicity and not being subjective to polygon determination. Once the rectangle is determined, lines may be drawn arbitrarily in both vertical and horizontal directions. In each rectangular grid, the background rate is assumed homogeneous. If the complete region is partitioned into 100 square regions with each direction portioned into 10 segments, we have 100 grids and the complete rectangular region is considered inhomogeneous in space. The number 100 is chosen only for easy understanding and simple computation. The software has the capability to adjust for other possible grid partitions. In the process of model building, we use four variations of square grid partitions and show that model fitting is improved when number of square grids is large enough. Using the values of log-likelihood, we determine the best models among these five models. Including the homogeneous model, we will compare such partitions of five different models. Their abbreviated names are used as follows throughout this chapter:

1. Homogeneous models  $M_H$ .  $\mu(x, y)$  are a constant over the entire region.
2. Inhomogeneous model  $M_{125}$  with 25 grids, each grid is  $2^\circ$  in longitude by  $2^\circ$  in latitude.  $\mu(x, y)$  is a constant within one grid. There are 25 parameters of  $\mu(x, y)$  to be computed.
3. Inhomogeneous model  $M_{1100}$  with 100 grids, each grid is  $1^\circ$  in longitude by  $1^\circ$  in latitude.  $\mu(x, y)$  is a constant within one grid. There are 100 parameters of  $\mu(x, y)$  to be computed.
4. Inhomogeneous model  $M_{1400}$  with 400 grids, each grid is  $0.5^\circ$  in longitude by  $0.5^\circ$  in latitude.  $\mu(x, y)$  is a constant within one grid. There are 400 parameters of  $\mu(x, y)$  to be computed.
5. Inhomogeneous model  $M_{11600}$  with 1600 grids, each grid is  $0.25^\circ$  in longitude by  $0.25^\circ$  in latitude.  $\mu(x, y)$  is a constant within one grid. There are 1600 parameters of  $\mu(x, y)$  to be computed.

The Akaike's information criterion (AIC; Akaike 1974) is widely used and convenient statistically for model comparison. We apply the Akaike's information criterion (AIC) to evaluate each model for model diagnosis. Smaller values of AIC indicate better-fit models. Here,

$$\text{AIC} = -2\max(\log - \text{likelihood}) + 2(\text{number of adjusted parameters}).$$

### 7.4 Results

Table 7.1 shows the ETAS modeling results from MLEs of homogeneous background rate of  $M_H$  and triggering parameters of the five models. We observe that there is no pronounced discrepancy among the estimates of triggering parameters for these models.  $M_{1100}$  appears to have the best fit among all models, according to AIC. Unsurprisingly,  $M_{1400}$  and  $M_{11600}$  are indeed over-fitting models since the catalog’s sample size is 2009, and it is close to  $2 \times$  (number of adjusted parameters). The number of adjusted parameters differs by models:  $M_H$  contains seven parameters (one background rate and six triggering parameters);  $M_{125}$  contains 31 parameters (25 background rate and six triggering parameters);  $M_{1100}$  contains 106 parameters (100 background rate and six triggering parameters), etc. According to their AIC values,  $M_H$  and  $M_{125}$  do not fit as well as  $M_{1100}$ ,  $M_{1400}$  and  $M_{11600}$ .

The background rates of all five models  $M_H$ ,  $M_{125}$ ,  $M_{1100}$ ,  $M_{1400}$  and  $M_{11600}$  are displayed in Fig. 7.3. In all of the inhomogeneous models, unsurprisingly, grids with more events, especially clusters, have larger background rates than those grids having sparse events. The highest background rates occur around the bottom-left part of Longmenshan fault, where the 2008 Wenchuan  $M7.9$  earthquake occurred.

Predicted intensity rate is calculated according to Eq. (7.2) for all five models. Figure 7.4a and b shows the predicted intensity rate  $\lambda$  of models  $M_H$  and  $M_{125}$ . Grids with more events have higher predicted intensity rate. The intensity rate  $\lambda$  of models  $M_{1100}$ ,  $M_{1400}$ , and  $M_{11600}$  appears alike to the predicted intensity rate  $\lambda$  of  $M_H$  and  $M_{125}$  (omitted in figure), but they are not identical. We compute the difference  $\lambda_{125} - \lambda_H$

**Table 7.1** ETAS MLE results obtained using the homogeneous model  $M_H$  and inhomogeneous models  $M_{125}$ ,  $M_{1100}$ ,  $M_{1400}$ , and  $M_{11600}$

Homogeneous	Model $M_H$	$(\alpha, c, d, K_0, p, q, \mu) = (1.028, 0.0789, 0.0149, 1.488E-4, 1.246, 2.160, 2.666E-4)$ Log-likelihood = -5719; AIC = 11,440
Inhomogeneous	Model $M_{125}$	$(\alpha, c, d, K_0, p, q) = (1.047, 0.0704, 0.0152, 1.308E-4, 1.246, 2.184)$ Log-likelihood = -1583; AIC = 3215
	Model $M_{1100}$	$(\alpha, c, d, K_0, p, q) = (1.047, 0.0826, 0.0149, 1.349E-4, 1.270, 2.184)$ Log-likelihood = -254; AIC = 707
	Model $M_{1400}$	$(\alpha, c, d, K_0, p, q) = (1.066, 0.0752, 0.0154, 1.207E-4, 1.270, 2.207)$ Log-likelihood = -32; AIC = 863
	Model $M_{11600}$	$(\alpha, c, d, K_0, p, q) = (1.066, 0.0808, 0.0160, 1.084E-4, 1.293, 2.254)$ Log-likelihood = 1138; AIC = 924

Each model’s log-likelihood and AIC are given. Computation tolerance is 0.001. Smaller AIC indicates better fit. We can see from AIC that  $M_{1100}$  fits better than other models. The models  $M_{1400}$ , and  $M_{11600}$  are not better due to large number of parameters, and the penalty is applied in AIC

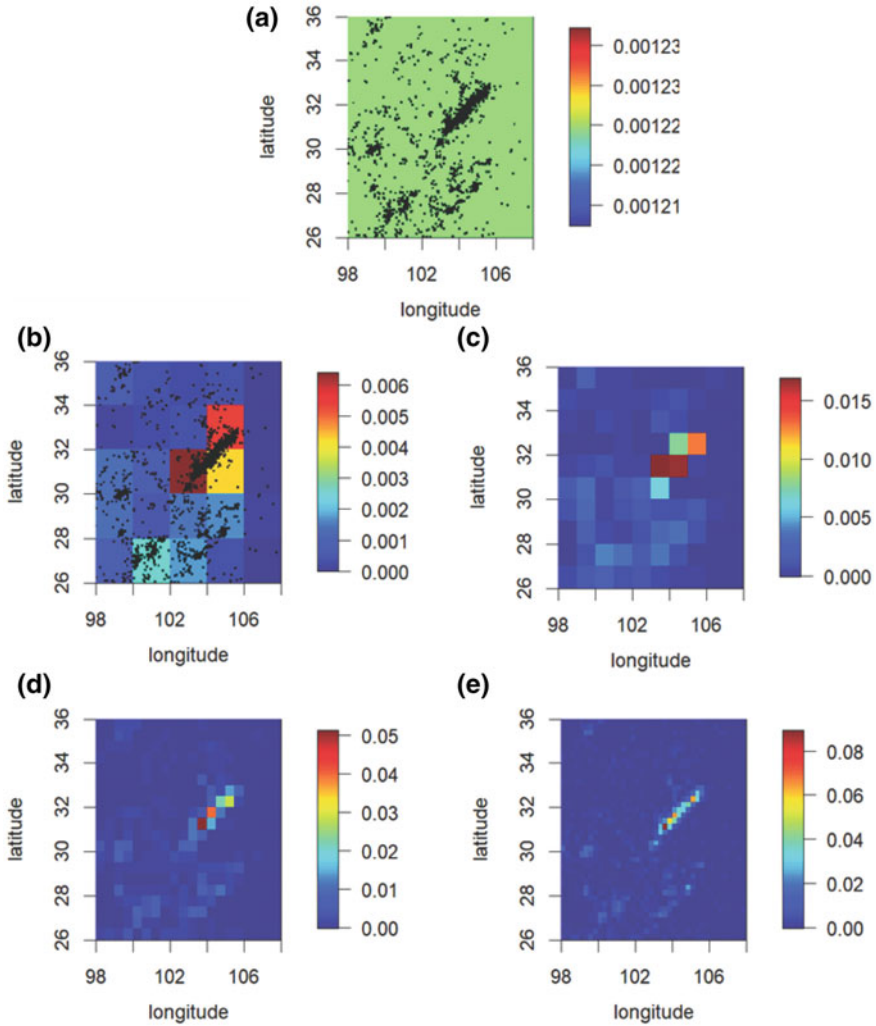


**Fig. 7.3** **a** Homogeneous background rate of model  $M_H$  displayed with events. Constant background rate  $\mu = 2.666E-4$ . **b** Inhomogeneous background rate of  $M_{125}$  displayed with events. Grids with higher background intensity rates are the three neighborhood grids of the Wenchuan event, which is part of the Longmenshan fault seismic cluster. The grid including the Wenchuan event has the highest background intensity rate. **c** Inhomogeneous background rate of  $M_{1100}$ , **d**  $M_{1400}$  and **e**  $M_{11600}$  displayed with events. Events are not displayed for clarity of the grids. Difference between the clustered regions and sparse regions is larger when number of grids increases



and demonstrate it in Fig. 7.4c.  $\lambda_{125}$  is greater than  $\lambda_H$  over the complete rectangular region. In area with sparse events, the difference is more pronounced. In area with clustered events, the difference is relatively smaller. Similar phenomenon appears in Fig. 7.4c–f, which respectively show the differences  $\lambda_{125} - \lambda_H$ ,  $\lambda_{1100} - \lambda_{125}$ ,  $\lambda_{1400} - \lambda_{1100}$  and  $\lambda_{11600} - \lambda_{1400}$ . We have observed that  $\lambda_{11600} > \lambda_{1400} > \lambda_{1100} > \lambda_{125} > \lambda_H$ . The predicted intensity rate is larger when a inhomogeneous model with more grids is used. The difference between two models with larger number of grids, for example,  $M_{1400}$  and  $M_{11600}$ , tends to be larger than difference between two models with fewer grids, for example,  $M_{125}$  and  $M_H$ . In summary, by observing the predicted intensity rate, the homogeneous model and models with few grids appear to underestimate the intensity rate. Models with large number of background grids appear to overestimate the intensity rate.

It is informative to compare the seismic activities before and after the Wenchuan event. We partition the data into two sub-catalogs: 1973/01/01–2008/05/08 excluding the Wenchuan event (we will call this time window  $TW_I$ ) and 2008/05/08 excluding the Wenchuan event (we will call this time window  $TW_{II}$ ). The time windows  $TW_I$  and  $TW_{II}$  have catalog sizes 690 and 1318, respectively. If we view the 45-year time window from 1973 to 2017 without partitioning it into  $TW_I$  and  $TW_{II}$ , it is not possible to observe the difference.  $TW_I$  is much larger than  $TW_{II}$ , but it has much lesser events. The seismic activities before and after Wenchuan event along Longmenshan fault are noticeably different. Events appear clustered in the southwest area in  $TW_I$ . It is unsurprising to learn that these two time windows produce distinct  $\alpha$  values as shown in Table 7.2, which summarizes the result of ETAS model fitting of catalogs in  $TW_I$  and  $TW_{II}$ .

The triggering parameters except  $\alpha$  are similar between the two time windows. However,  $\alpha$  has its value varying between the two time windows, and the values have noticeable difference from the  $\alpha$  values of models over the complete time window of 1973–2017, roughly around 1.03–1.07.  $\alpha$  is about 1.28 in  $TW_I$  and about 1.47 in  $TW_{II}$ , indicating that the seismicity is closer to swarm type in  $TW_I$ , but is more clustered in  $TW_{II}$ . As described in Sect. 7.3, ETAS models give the parameter MLEs and they have physical meanings. Besides the abovementioned parameter  $\alpha$  that is related to seismicity types, the parameters  $c$  and  $p$  are related to how an event is affected by previous events in time.  $c$  of  $TW_I > c$  of  $TW_{II}$  and it indicates that in  $TW_I$ , temporal decay is larger and more gradual in time as an event moves away from the mainshock, and in  $TW_{II}$ , temporal decay is relatively smaller. However, their difference is small.  $p$  of  $TW_I < p$  of  $TW_{II}$  indicates that  $TW_I$  has longer and gradual time decay and  $TW_{II}$  has shorter and sharper time decay, which coincide with the conclusion drawn by the  $c$  values. Their difference is also small. Similarly, the parameters  $d$  and  $q$  are related to how an event is affected by previous events in space.  $d$  of  $TW_I > d$  of  $TW_{II}$  indicates that in  $TW_I$ , spatial decay is larger and gradual as an event moves further from the mainshock, and in  $TW_{II}$ , spatial decay is relatively smaller. Their difference is also small.  $q$  of  $TW_I < q$  of  $TW_{II}$  indicates that  $TW_I$  has longer and gradual spatial decay and  $TW_{II}$  has shorter and sharper spatial decay, which coincide with the conclusion drawn by the  $d$  values. In summary, events in  $TW_{II}$  tend to have shorter influence temporally and spatially. The parameter  $K_0$

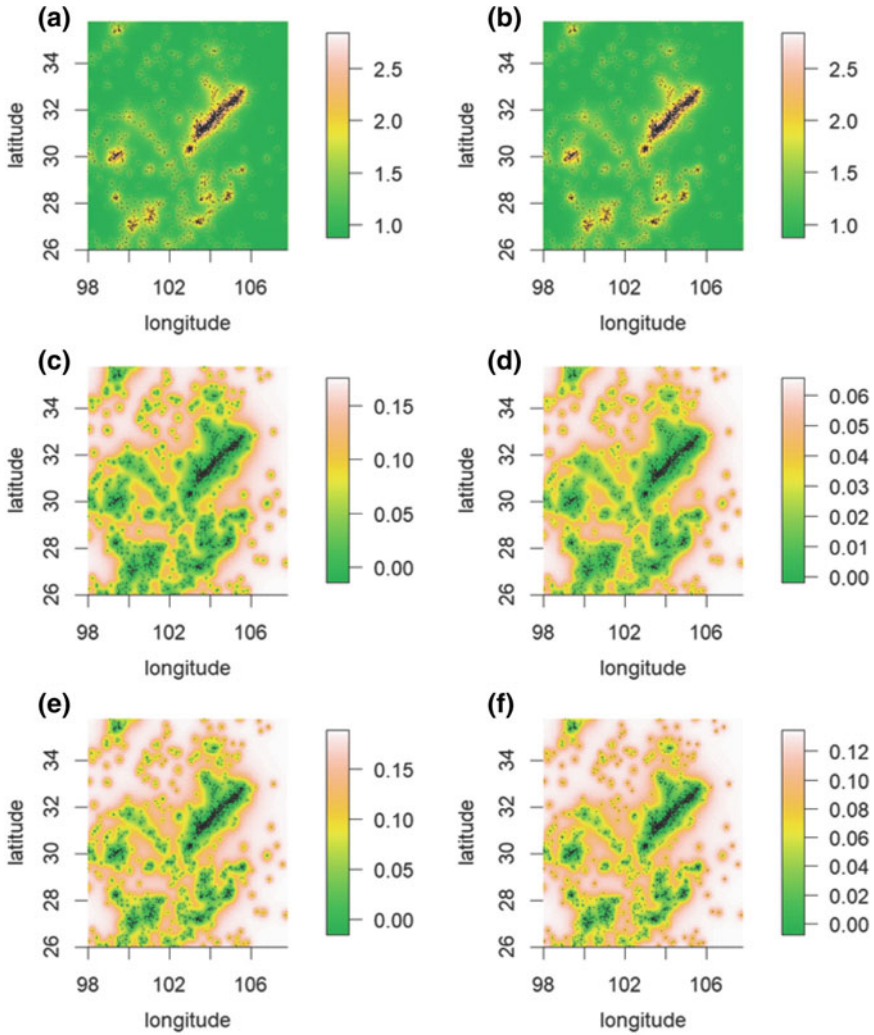


**Fig. 7.4** Predicted intensity **a**  $\lambda_H$  using the homogeneous model  $M_H$  and **b**  $\lambda_{I25}$  using the inhomogeneous model  $M_{I25}$ , respectively, displayed with events. **c**  $\lambda_{I25} - \lambda_H$ , difference in predicted intensity between  $M_H$  and  $M_{I25}$ . **d**  $\lambda_{I100} - \lambda_{I25}$ , difference in predicted intensity between  $M_{I25}$  and  $M_{I100}$ . The difference is much less than the difference  $\lambda_{I100} - \lambda_H$ . **e**  $\lambda_{I400} - \lambda_{I100}$ , difference in predicted intensity between  $M_{I400}$  and  $M_{I100}$ .  $\lambda_{I400} > \lambda_{I100}$  over the entire rectangular region. The difference is more pronounced for area with clustered events and more pronounced for area with sparse events. **f**  $\lambda_{I1600} - \lambda_{I400}$ , difference in predicted intensity between  $M_{I100}$  and  $M_{I400}$ .  $\lambda_{I1600} > \lambda_{I400}$  over the entire rectangular region. The difference is less pronounced for area with clustered events and more pronounced for area with sparse events

**Table 7.2** ETAS MLE result of triggering parameters obtained using  $M_I$  and  $M_{II}$ . Both models have their  $\alpha$  much larger than the original time window (1973–2017)

$M_I$	$(\alpha, c, d, K_0, p, q) = (1.277, 0.0935, 0.0197, 7.869E-5, 1.246, 2.184)$
$M_{II}$	$(\alpha, c, d, K_0, p, q) = (1.468, 0.0811, 0.0152, 8.210E-5, 1.293, 2.324)$

governs the expected number of direct aftershocks triggered by earthquake  $i$ . Larger  $K_0$  in  $TW_{II}$  indicates that the expected number of direct aftershocks is slightly larger according to the ETAS model. The physical meaning of seismicity explained by the triggering parameters also coincides with background rate. The plots of events in Fig. 7.5a, indeed, show that in  $TW_I$ , the seismicity is mostly swarmed with moderate clusters around the bottom-left corner. In contrast, the seismicity in  $TW_{II}$  is noticeably clustered along the Longmenshan fault in Fig. 7.5b.

Table 7.3 shows the number of events roughly by years, with the first two rows indicating the number of events in 2008, before and after Wenchuan earthquake. The difference is tremendous. In 2008, there are only six events before the Wenchuan earthquake but 794 events after the Wenchuan earthquake. Among the 2009 shallow events from 1973 to 2017, 794 events within approximately eight months after the Wenchuan earthquake account for 39.5% of the seismic activity during 45 years. These events may dominate the estimation of parameter MLEs, especially the parameter, that are sensitive to change in data, such as  $\alpha$  and  $K_0$ .

It might be artificial to use year as grouping criterion; therefore, we provide the magnitude on time plot to depict the region’s seismicity from 1973 to 2017 in Fig. 7.6a. It is noted that  $TW_I$  has 12,889 days (approximately 35.3 years and 78% of the 45-year window) and 690 events (approximately 34% of the complete 45-year time window), while  $TW_{II}$  has 3505 days (approximately 9.6 years and 21% of the 45-year window) and 1318 events (approximately 66% of the complete 45-year time

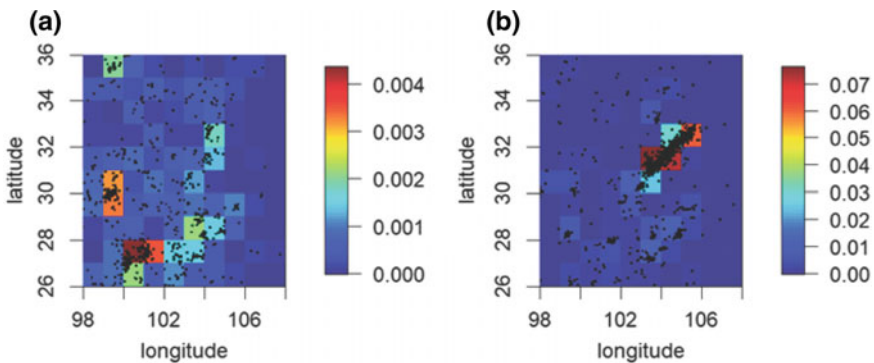


**Fig. 7.5** **a** Catalog of 609 events in  $TW_I$  modeled using  $M_{1100}$ . Inhomogeneous background rate is plotted with the events. **b** Catalog of 1318 events in  $TW_{II}$  modeled using  $M_{1100}$ . Inhomogeneous background rate is plotted with the events

**Table 7.3** Number of events by year in TW<sub>II</sub>

Time window	Number of events with magnitude $\geq 4.0$
2008/01/01–2008/05/08 (before and excluding Wenchuan event)	6
2008/05/08–2008/12/31 (after and excluding Wenchuan event)	794
2009/01/01–2009/12/31	46
2010/01/01–2010/12/31	34
2011/01/01–2011/12/31	44
2012/01/01–2012/12/31	41
2013/01/01–2013/12/31	132
2014/01/01–2014/12/31	79
2015/01/01–2015/12/31	45
2016/01/01–2016/12/31	103
2017/01/01–2017/12/31	48

window). We observe that the number of events shows a very noticeable variation. Right after the Wenchuan event, the density of events is much larger than other intervals for about eight months and this might be related to the clustered events along the Longmenshan fault.

We separate these two time windows and depict their seismicity. The events in TW<sub>I</sub> are displayed in Fig. 7.7a, where larger events are shown by larger circles. The seismicity appears clustered moderately in the southwest area, but not along the Longmenshan fault. The seismicity of TW<sub>II</sub> is displayed in Fig. 7.7b. Seismic clusters shown in Fig. 7.7a and b are not resembled indeed. To observe how the Wenchuan earthquake might have produced aftershocks, Fig. 7.7c shows 794 events from 2008/05/08 to 2008/12/31, excluding the Wenchuan earthquake. The events from 2009/01/01 to 2012/12/31 are shown in Fig. 7.7d while the events from 2013/01/01 to 2017/12/31 are shown in Fig. 7.7e. They all appear to be different in distribution of events in space. We can see that the Wenchuan earthquake appears to have tremendously influence the region's seismicity within a few months. The effect appears to last within approximately for more than four years. After four years, the cluster along Longmenshan fault is no longer pronounced as shown in Fig. 7.7e.

One might be curious if the Wenchuan event's seismicity is similar to later three large events: *M*6.6 Lushan event occurring on 2013/04/20, the *M*6.2 Ludian event occurring on 2014/08/03, and the *M*6.5 Jiuzhaigou event occurring on 2017/08/08. These events happened after the Wenchuan event, and they happened during the later time of TW<sub>II</sub>. They are part of the data analysis for all of the 45 years (1973–2017) and also part of TW<sub>II</sub> (2013/01/01 to 2017/12/31, which is a very short period to analyze). They do not seem to create significant clusters. The clusters after 2008/05/08 appear mostly related to the Wenchuan event. To see that the Lushan, Ludian, and Jiuzhaigou events' aftershocks are relatively more sparse than the aftershocks of the Wenchuan

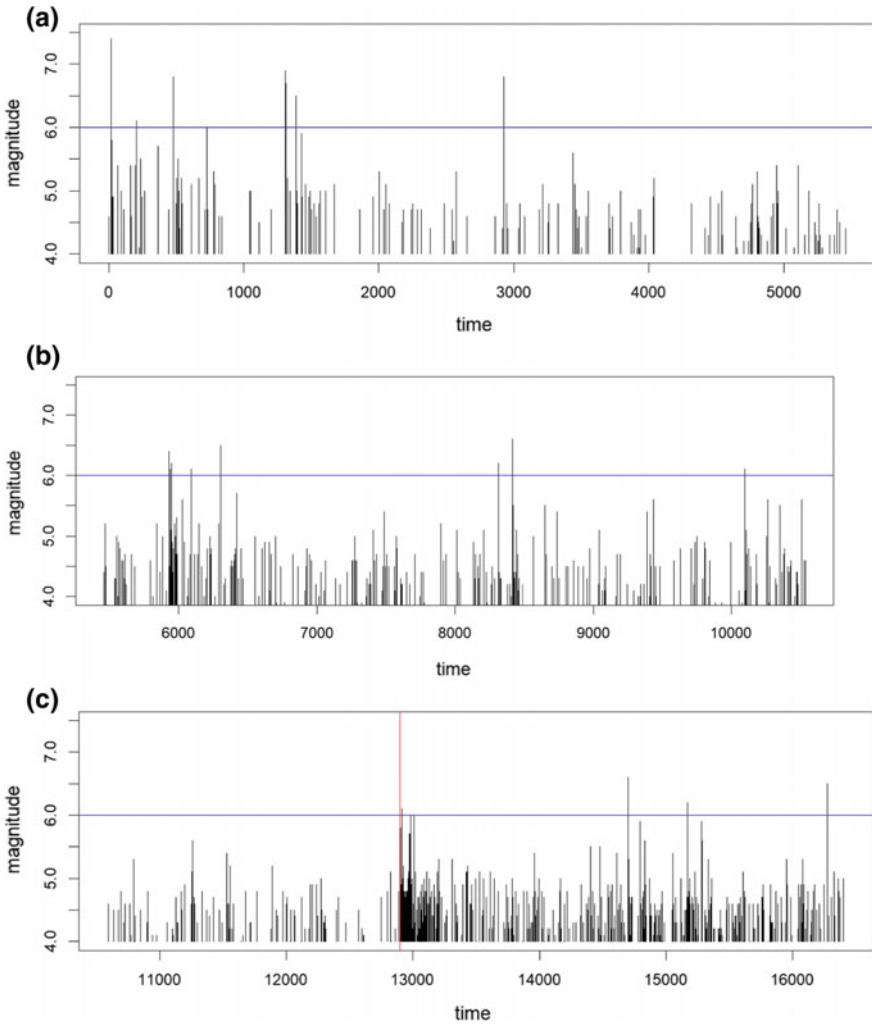


**Fig. 7.6** Plot of magnitude versus time. The horizontal axis indicates time in day, and the vertical axis indicates magnitude. The time interval is 45 years from 1973/01/01 to 2017/12/15, and time = 16,403 is the occurrence time of the last event. **a** Time window from 1973/01/01 to 1987/12/31 (15 years). **b** 1988/01/01–2002/12/31 (15 years). **c** 2003/01/01–2017/12/31 (15 years), which contains the Wenchuan event. The three large events in the same figure as the 2008 M7.9 Wenchuan (marked by red vertical line) events are Lushan, Ludian, and Jiuzhaigou events. The Wenchuan event appears to have noticeably more aftershocks with magnitude  $\geq 4.0$  than the other three events

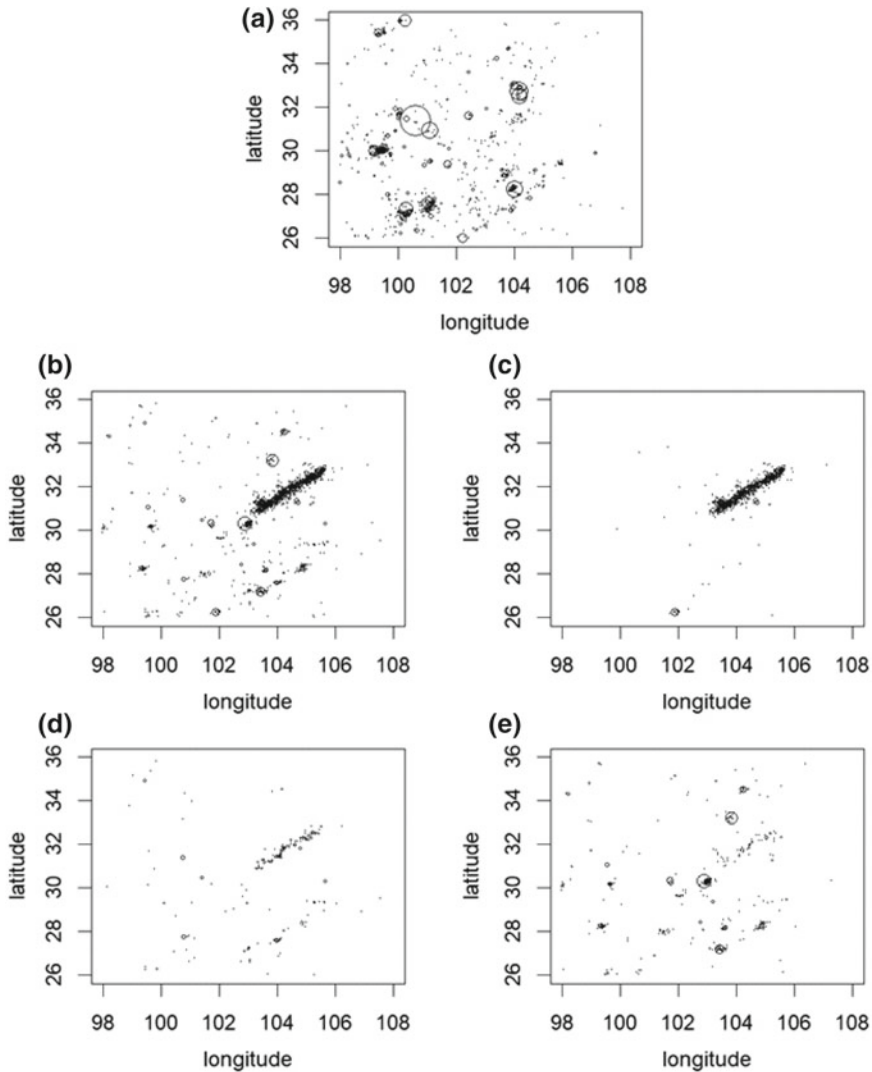


**Fig. 7.7** **a** Events in  $TW_I$ . The largest event is the Luhuo earthquake. The Wenchuan earthquake is not displayed in this figure. **b** Events in  $TW_{II}$  from 2008/05/08 to 2017/12/31. There are 1318 events. Clustered events along the Longmenshan fault is shown clearly. The Wenchuan earthquake is not displayed in this figure. **c** Events in part of  $TW_{II}$  from 2008/05/08 to 2008/12/31. There are 794 events. Clustered events along the Longmenshan fault is shown clearly. The Wenchuan event is not displayed in this figure. **d** Events in part of  $TW_{II}$  from 2009/01/01 to 2012/12/31. There are 165 events. Clustered events are obvious along the Longmenshan fault. **e** Events in part of  $TW_{II}$  from 2013/01/01 to 2017/12/31. There are 359 events. Clustered events are not as pronounced as in the time window from 2008/05/08 to 2012/12/31. There are only three events with magnitude  $\geq 6.0$ : Lushan event occurring at  $30.308^\circ\text{N}$ ,  $102.888^\circ\text{E}$  on 2013/04/20, with magnitude 6.6, and it is close to the Wenchuan earthquake epicenter, the Ludian event occurring at  $27.1891^\circ\text{N}$ ,  $103.4086^\circ\text{E}$  on 2014/08/03 with magnitude 6.2, and the Jiuzhaigou event occurring at  $33.1926^\circ\text{N}$ ,  $103.8552^\circ\text{E}$  on 2017/08/08, with magnitude 6.5

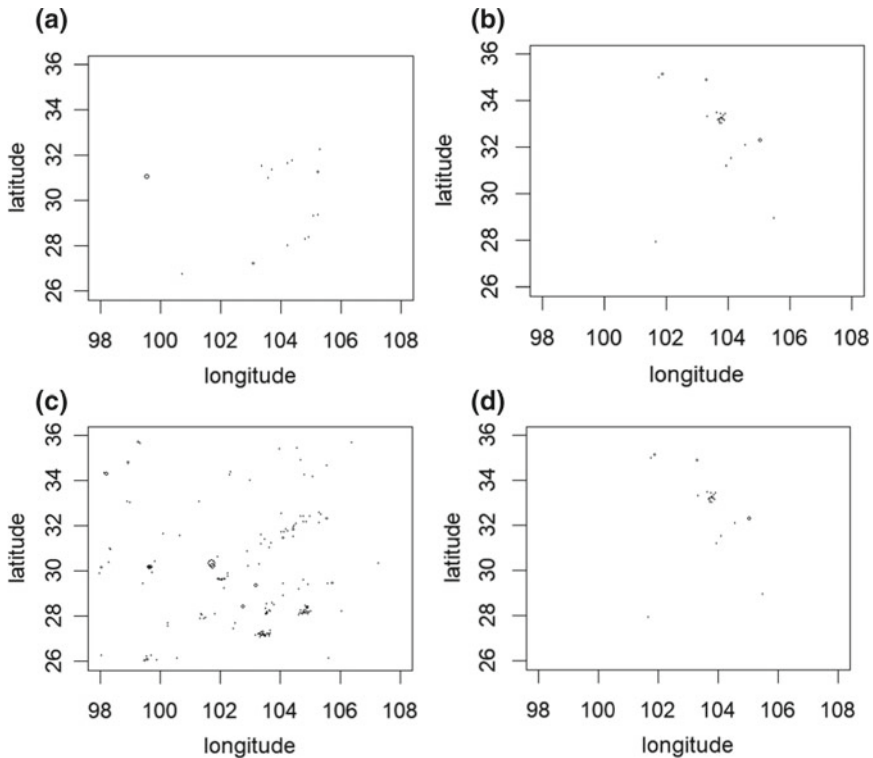


**Fig. 7.8** Plots show the seismicity for **a**  $TW_{III}$ , **b**  $TW_{IV}$ , **c**  $TW_V$ , and **d**  $TW_{VI}$

event, we will define time windows and describe their seismicity,  $TW_{III}$ : 2013/01/01 to 2014/04/20 before Lushan event (excluding Lushan quake),  $TW_{IV}$ : 2014/04/20 to 2014/08/03 after Lushan event before Ludian event (excluding Lushan and Ludian quakes),  $TW_V$ : 2017/08/08 after Ludian event before Jiuzhaigou event (excluding Ludian and Ludian quakes), and  $TW_{VI}$ : 2017/08/08 to 2017/12/31 after Jiuzhaigou event (excluding Jiuzhaigou quake). Figures 7.8 and 7.9 provide spatial and time plots made for these time windows, and we can see that the aftershock patterns of the later three large events do not act similar to the Wenchuan event, although data might be too few to conclude for Jiuzhaigou event (2017/08/08). Wenchuan event's aftershocks also appear differently from the Luhuo event in 1973. Although it is commonly observed that numerous aftershocks occur after a large event, the Wenchuan event appears to have more aftershocks with magnitude  $\geq 4.0$  according to Fig. 7.6.

We also provide the data of Southern California for a comparison. Figure 7.10 shows the seismic data of Southern California in rectangular region  $[112^\circ W, 124^\circ W]$  in longitude by  $[30^\circ N, 38^\circ N]$  in latitude, from 1973/01/01 to 2015/12/31. The survivor plot in Fig. 7.11 shows that the data are complete for magnitude  $\geq 3.0$ , and we

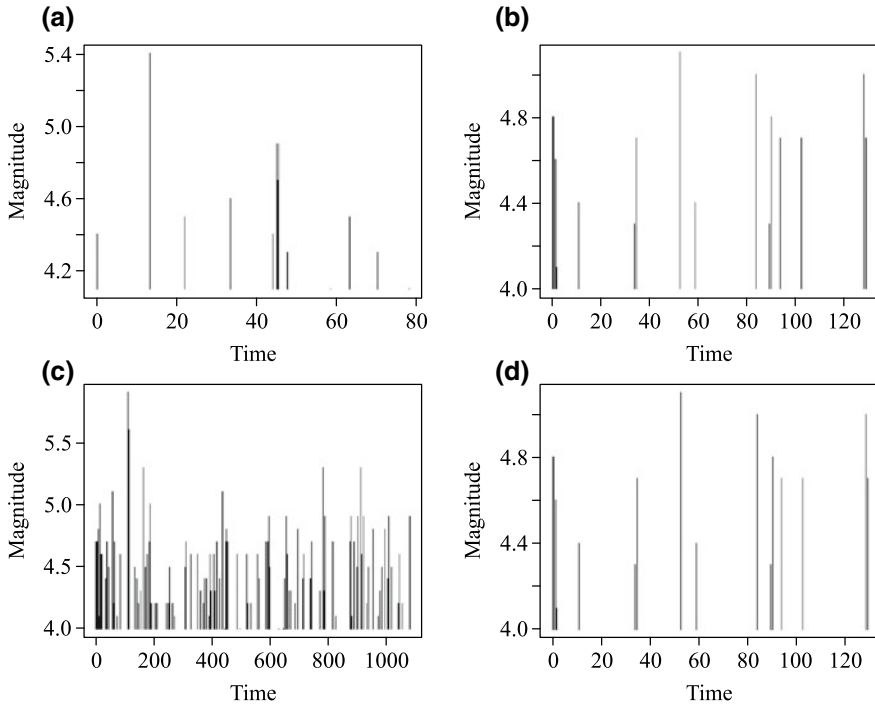
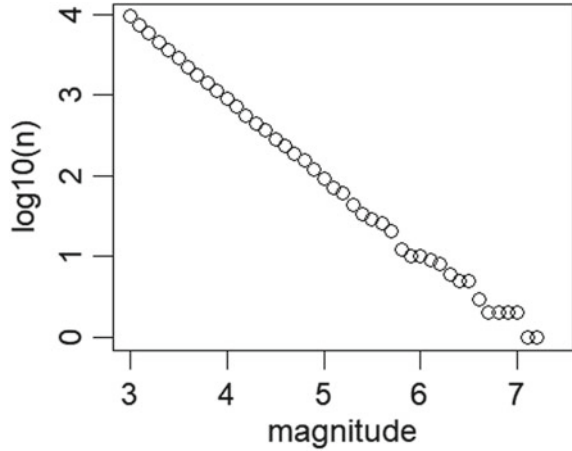


**Fig. 7.9** Plots of magnitude versus time for **a**  $TW_{III}$ , **b**  $TW_{IV}$ , **c**  $TW_V$ , and **d**  $TW_{VI}$

include all data with magnitude  $\geq 3.0$  in Fig. 7.10. We can observe that not all the large events with magnitude  $\geq 6.0$  have similar foreshock and aftershock patterns. Some large events are more clustered, and some have longer decay than others. Those similar on aftershocks with magnitude  $\geq 4.0$  may appear differently on aftershocks with magnitude  $< 4.0$ . Since the Wenchuan region is not complete for magnitude interval between 3.0 and 4.0, it is difficult to compare Wenchuan event's aftershocks below 4.0 with other large event's aftershocks below 4.0. However, the Wenchuan event has noticeably more aftershocks with magnitude  $\geq 4.0$  than Southern California's Landers, Hector Mine, and Baja California events as shown in Fig. 7.11. Before the Wenchuan event, foreshocks are observed. Before the foreshocks, a period of time shows serenity. In Fig. 7.6, we also see that there are lesser events before the Wenchuan event—a quiet period of time and few foreshocks for about 500 days. In contrast, three large events after 2008 do not show the same foreshock and aftershock patterns.



**Fig. 7.10** Survivor curve of Southern California earthquake data with minimum magnitude cutoff 3.0, from 1973/01/01 to 2015/12/31, in rectangular space  $[-124, -112]$  in longitude by  $[30, 38]$  in latitude. There are 11,684 events. The plot of  $\log_{10}(n)$  on magnitude is linear, and this shows near completeness of catalog with minimum magnitude cutoff 3.0



### 7.5 Simulation

In this section, we demonstrate simulation using the estimated parameters by ETAS model. Simulation provides the benefit of calculating standard errors of the parameters. The inhomogeneous model  $M_{1100}$  is used for our simulation demonstration. The simulation process consists of two stages: generation of background events and triggered events. For each simulated catalog, the data of 2009 events in 1973/01/01 to 2017/12/31 are used to stochastically determine which events are included in the simulated catalog as background events. The background events are kept in the simulated catalog, and their aftershocks are generated. Each background event will have a number of aftershocks. There are four variables to simulate for each aftershock event in a simulated catalog: longitude, latitude, time, and magnitude. The simulation mechanisms of the four variables are described below:

- The time of an event is uniformly generated within the time window.
- Longitude ( $x$ ) and latitude ( $y$ ) are uniformly generated spatially. For an inhomogeneous model, they are generated within a grid.
- Magnitude of the  $i$ -th event is generated by:

$$m_i = m_{GR} - \ln(1 - r(1 - \exp(-\beta(M_{GR} - m_{GR}))))/\beta$$

where  $\beta$  denotes the Gutenberg–Richter branching ratio described in Sect. 7.2.  $r$  is a uniform random number,  $0 < r < 1$ .  $M_{GR}$  and  $m_{GR}$  denote Gutenberg–Richter’s maximum and minimum magnitudes, respectively. Such limits are applied because an exponential distribution of earthquake magnitudes would make extremely strong earthquakes more likely than they actually occur. Therefore, a truncated exponential distribution is used, which sets a specified maximum for simulated earthquake events (Veen and Schoenberg 2008). In our study, they are set to be  $m_{GR} = 4.0$  and  $M_{GR} = 10.0$ .

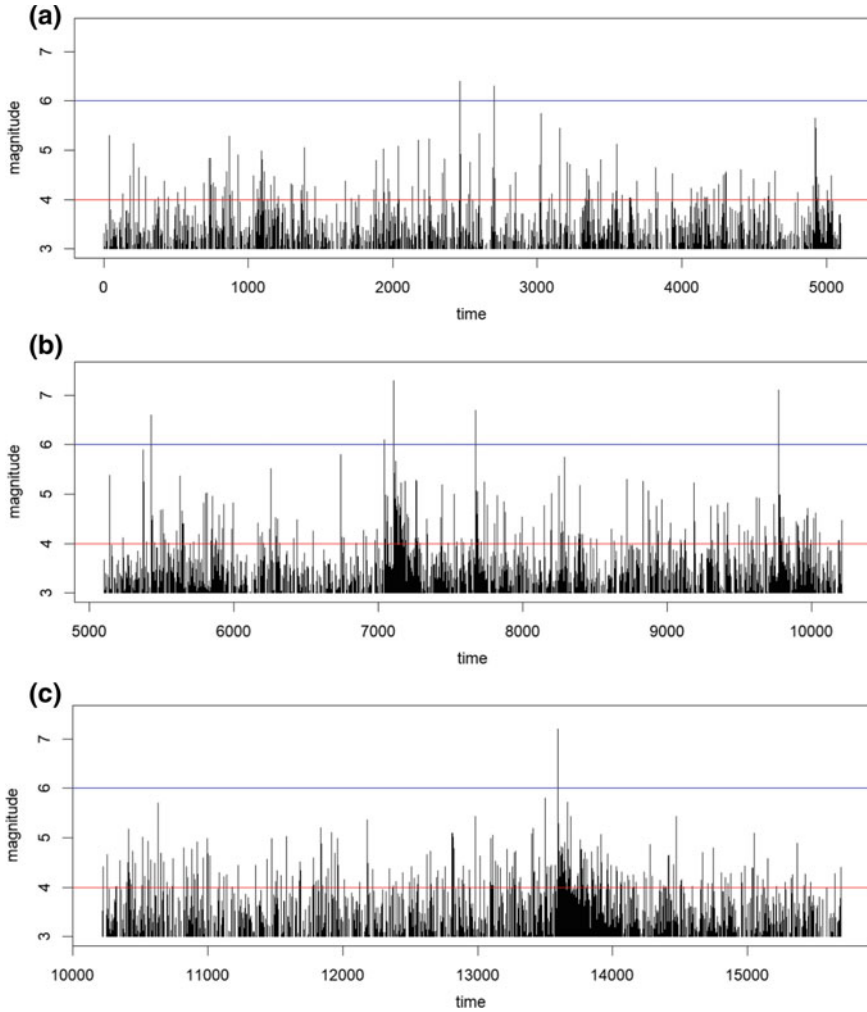


**Fig. 7.11** Plots of magnitude versus time for Southern California earthquake data of 11,684 events over 43 years. **a** Time window from 1973/01/01 to 1986/12/31 (14 years). **b** 1987/01/01–2000/12/31 (14 years). **c** 2001/01/01–2015/12/31 (15 years). We observe that the patterns of foreshocks and aftershocks differ for large events with magnitude  $\geq 6.0$ : Some appear to have lots of foreshocks below magnitude 3.0 but not above 4.0. Some have almost no foreshocks with magnitude 3.0. Some large events have many more aftershocks  $\geq 4.0$  than other events. The event at time approximately = 7300 days is the  $M7.3$  Landers event (1992/06/28). The event at time approximately close to 10,000 days is the  $M7.2$  Hector Mine event (1999/10/16). The event at time between time 13,000 and 14,000 is the  $M7.1$  Baja California event (2010/04/04). Both the Landers and Baja California events appear to have numerous aftershocks, but the later one has more aftershocks with magnitude between 3.0 and 4.0, over longer period of time

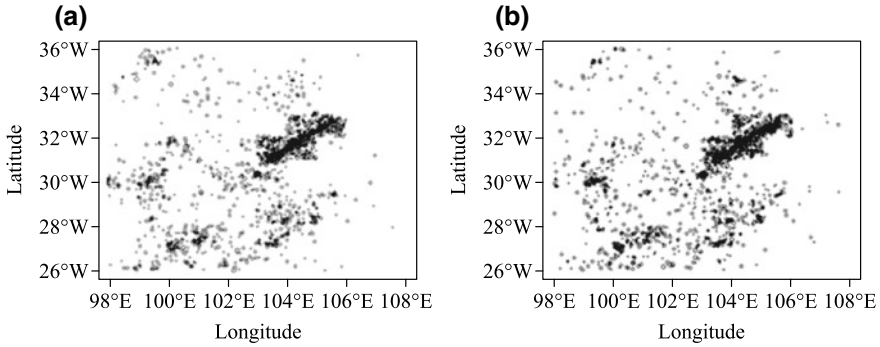


**Fig. 7.12** **a** and **b** are two examples of simulation using model  $M_{1100}$ . All 30 simulated catalogs have their spatial distributions similar to these two examples

A thinning process is implemented in event generation. The expected number of first-generation events is calculated using the parameters  $(\alpha, c, d, K_0, p, q)$ :

$$G_i(\theta) = \int_0^\infty \int_{-\infty}^\infty \int_{-\infty}^\infty g(t - t_i, x - x_i, y - y_i, m_i) dx dy dt = \pi K_0 \frac{c^{-\omega}}{\omega} \frac{d^{-\rho}}{\rho} e^{\alpha(m_i - M_0)} \tag{7.4}$$

Using 30 simulated catalogs, we have computed the standard error for each triggering parameter. Most of the simulated catalogs have catalog size between 1700 and 2400. Figure 7.12 shows examples of simulation using MLEs of  $M_{1100}$ . Two examples of time versus magnitude plot are displayed in Fig. 7.13. All simulated catalogs are similar to these two examples and have magnitude cutoff  $M_0 = 4.0$ . The standard errors and 95% confidence intervals of  $M_{1100}$ 's triggering parameters are given below.

$$\begin{aligned} \widehat{SE}_\alpha &= 0.114, 95\% CI_\alpha = (0.819, 1.274) \\ \widehat{SE}_c &= 0.000134, 95\% CI_c = (0.823, 0.829) \\ \widehat{SE}_d &= 0.000116, 95\% CI_d = (0.0147, 0.0151) \\ \widehat{SE}_{K_0} &= 1.81E-05, 95\% CI_{K_0} (9.88E-05, 1.17E-04) \\ \widehat{SE}_p &= 0.00485, 95\% CI_p = (1.26, 1.28) \\ \widehat{SE}_q &= 0.00831, 95\% CI_q = (2.17, 2.20) \end{aligned}$$

The parameters  $c, d, p,$  and  $q$  appear to have small standard errors with respect to their estimates. These parameters are indeed those that have smaller variations among model fitting in not only Wenchuan data, but also in Southern California and global data. In contrast, the parameters  $\alpha$  and  $K_0$  have larger standard errors with respect to their estimates.  $K_0$  is a parameter that has large variation with respect to its

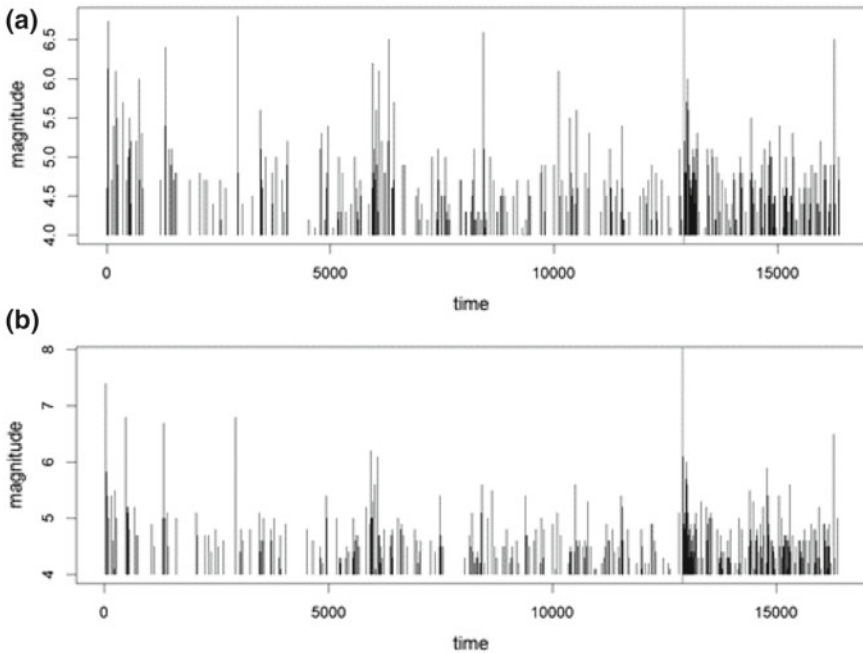


**Fig. 7.13** **a** and **b** Plots of magnitude versus time for simulated examples of Fig. 7.12, using model  $M_{1100}$ . The highest vertical line indicates the time of the 2008  $M_{7.9}$  Wenchuan earthquake

estimate due to the flatness of convergence plane of maximum likelihood estimation (Veen and Schoenberg 2008).  $\alpha$  is a parameter that is relatively difficult to estimate and may suffer the scenario of divergence in estimation (Chu 2018), which has worse convergence than parameter  $K_0$ .  $\alpha$  is more sensitive to data than  $K_0$ . The aftershocks within months after the Wenchuan earthquake account for about 39.5% of the 2009 events and might play a crucial role for the calculation of  $\alpha$ .

We also have obtained the standard errors and confidence interval for some of the background rates. The summary statistics of 30 standard errors of background rates  $\mu(x, y)$  are: minimum = 0,  $Q_1 = 0.000120$ , median = 0.000479, mean = 0.000949,  $Q_3 = 0.00143$ , and maximum = 0.00479. The minimum is 0 because there are grids with no events. Figure 7.14 depicts the distribution of the background rates. The background rate grids with highest standard errors at the histogram's right tail come from the grids of the middle part of Longmenshan fault (approximately 31.5°N, 104.5°E) and the bottom area of the region. Simulated catalogs have larger variation in these sub-regions due to these regions' larger variation of seismicity. The grids with more points tend to have larger standard errors. Some of the grids have their standard errors being 0 due to lacking any event.

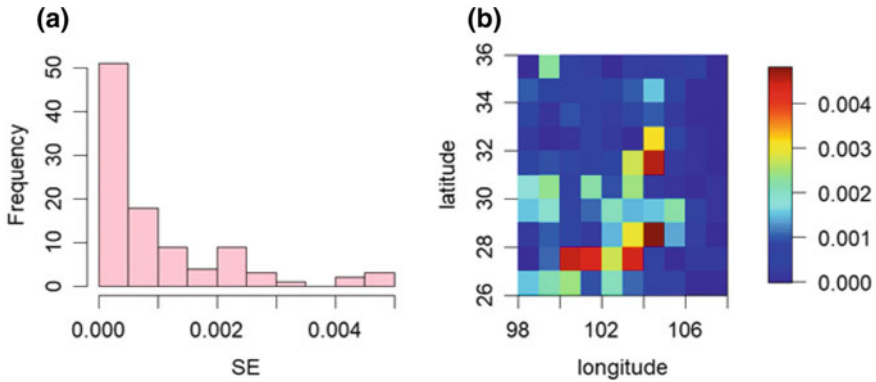


**Fig. 7.14** **a** Histogram showing the distribution of standard errors. Most grids have standard errors 0 or close to 0 due to their sparseness. **b** Graph to show the standard errors of background rate  $\mu(x, y)$

## 7.6 Conclusion

We have demonstrated estimation of inhomogeneous background rate with ETAS model, using simple rectangular grids and shown that among the models we tested, the inhomogeneous model  $M_{I100}$  fits better than the other four models. It is reasonable to understand that the homogeneous model  $M_H$  lacks adequacy to explain the seismic data of Wenchuan region, and models with numerous background rate parameters like  $M_{I400}$  and  $M_{I1600}$  are not optimal due to over-fitting the catalog of 2009 events. It should also be remarked that all the models triggering parameters' MLEs are similar comparing to triggering parameters of Southern California data and global data of the same zone 1. ETAS parameter MLEs can help us build predicted intensity rate like Fig. 7.4a and b. It makes possibility to visualize the region and sub-regions' intensity rates. We have also discovered that the seismic activity of Wenchuan vicinity changes over the 45 years from 1973 to 2017, and the seismicity appears noticeably different in scatter plots and model's MLEs. Additionally, as we have observed from the events of Wenchuan, Lushan, Ludian, and Jiuzhaigou, as well as Southern California's large earthquakes, foreshocks and aftershock pattern may be noticeably different and incompleteness of data is an important factor to consider.

To conclude the chapter, we raise four questions for our future study:

- It should be noted that the model  $M_{I100}$  is chosen for computation convenience, and a more optimal model may exist around 100 grids between 25 and 400 grids. Non-square grid partitions may also be implemented. Such grid partition may be also compared with other types of inhomogeneous approach, for example, irregular polygons along the Longmenshan fault, to identify an optimal model that may be easily generated by our software.
- It is observed that the time constants  $c$  and  $p$  have very small standard errors. Such phenomenon appears not only in analysis presented in this chapter, but also

in ETAS models' maximum likelihood estimation in general. While computation can be cumbersome, time-consuming, and unstable for ETAS MLE computation, we seek for solutions to attain more stable computation. Two questions are raised: Can we compute the time constants  $c$  and  $p$  by estimating the time model first, and then we use the estimated  $c$  and  $p$  as fixed values in the time-space model? Will such alternation make the computation for  $\alpha$ ,  $K_0$ ,  $d$  and  $q$  more stable?

- Our sub-catalogs of  $TW_I$  and  $TW_{II}$  have tremendous difference in seismicity. The seismicity within  $TW_{II}$  varies approximately every four to five years. It is worthwhile for further study if the serenity along Longmenshan before the Wenchuan event (Fig. 7.6) is related to the Wenchuan earthquake. In general, we should be aware that when different time window intervals are applied to the same region, we might obtain different MLE results to explain the region's seismicity differently since some parameters such as  $\alpha$  and  $K_0$  are sensitive to small variation of data. Such procedure is worthwhile to consider for seismic research.
- It is noted that the PDE catalog is incomplete for magnitude  $<4.0$ . By applying simulation, we can extend our work to simulate catalogs with lower magnitude cutoff, e.g.,  $M_0 = 3.0$  or lower to investigate how seismicity modeling may be improved. As previously mentioned in this chapter, some triggering parameters such as  $c$ ,  $d$ ,  $p$  and  $q$  are stable in estimation, and their standard errors are small compared to parameters  $\alpha$  and  $K_0$ . Simulation can help us understand how they are sensitive to data, improve our estimation for their MLEs, and find ways to eliminate bias. Simulations along with estimated ETAS parameters may also help us understand the missing data issue of incomplete magnitude  $<4.0$ .

**Acknowledgements** I am grateful to Dr. Yong-Gang Li, the editor-in-chief of this special volume, for his warm invitation and helpful suggestions to make this chapter possible.

## References

- Akaike, H. 1974. A new look at the statistical model identification. *IEEE Trans. Autom. Control*, AC-19, 716–723.
- Bird, P. 2003. An updated digital model of plate boundaries. *Geochem. Geophys. Geosyst.* 4 (3): 1027. <https://doi.org/10.1029/2001GC000252>.
- Chu, A., F.P. Scheenberg, P. Bird, D.D. Jackson, and Y.Y. Kagan. 2011. Comparison of ETAS parameter estimates across different global tectonic zones. *Bull. Seismol. Soc. Am.* 101 (5): 2323–2339.
- Chu, A. 2018. Comparisons of ETAS models on global tectonic zones with computing implementation. In *Chapter 4 of Fault-zone guided wave, ground motion, landslides and earthquake forecast*, ed. Y.-G. Li, 136–159. Beijing: Higher Education Press.
- Guo, Y., J. Zhuang, and S. Zhou. 2015. An improved space-time ETAS model for inverting the rupture geometry from seismicity triggering. *J. Geophys. Res.: Solid Earth*, 120 (5): 3309–3323, <https://doi.org/10.1002/2015jb011979>.
- Jiang, C.S., and J.C. Zhuang. 2010. Evaluation of background seismicity and potential source zones of strong earthquake in the Sichuan-Yunan region bae on the space-time ETAS model. *Chin. J. Geophys. (in Chinese)*, 53 (2): 305–317. 10.3969/j.issn. 0001-5733. 2010.02.008.

- Ogata, Y. 1988. Statistical models for earthquake occurrences and residual analysis for point processes. *J. Am. Stat. Assoc.* 83: 9–27.
- Ogata, Y. 1998. Space-time point process models for earthquake occurrences. *Ann. Inst. Stat. Math.* 50: 379–402.
- Ogata, Y. 2011. Significant improvements of the space-time ETAS model for forecasting of accurate baseline seismicity. *Earth Planets Space* 63: 217–229.
- Utsu, T., Y. Ogata, and R.S. Matsu'ura. 1995. The centenary of the Omori formula for a decay law of aftershock activity. *J. Phys. Earth* 43: 1–33.
- Veen, A. 2006. Some methods of assessing and estimating point processes models for earthquake occurrences. Ph.D. thesis, University of California, Los Angeles.
- Veen, A., and F.P. Schoenberg. 2005. Assessing spatial point process models for California earthquakes using weighted K-functions: analysis of California earthquakes. In *Case studies in spatial point process models*, ed. A. Baddeley, P. Gregori, J. Mateu, R. Stoica, and D. Stoyan, 293–306. NY: Springer.
- Veen, A., and F. Schoenberg. 2008. Estimation of space-time branching process models in seismology using an EM-type algorithm. *J. Am. Stat. Assoc.* 103 (482): 614–624.